Desalination and Water Treatment
www.deswater.com

doi: 10.5004/dwt.2023.29670

299 (2023) 190–202
July

One-step synthesis of biocarbon based nano zero-valent iron for efficient Rhodamine B removal in Fenton-like reactions

Zhongliang Shi†, Yi Dong†, Yiwen Chen, Bo Wang*, Haibo Wang*

Liaoning Engineering Research Center for Treatment and Recycling of Industrially Discharged Heavy Metals, Shenyang University of Chemical Technology, Shenyang 110142, China, emails: buang1996@163.com (B. Wang), wanghaibo@syuct.edu.cn (H.B. Wang), shzhl2000@163.com (Z.L. Shi), 841344608@qq.com (Y. Dong), 2016521218@qq.com (Y.W. Chen)

Received 24 March 2023; Accepted 5 June 2023

ABSTRACT

Organic pollutants in wastewater became a major challenge in the field of environmental remediation. In this work, biochar-loaded nano zero-valent iron (BC@nZVI) was successfully prepared and used to activate persulfate (PS) for Rhodamine B (RhB) removal from water. The structure and morphology of the nanocomposites were characterized by scanning electron microscopy equipped with energy-dispersive X-ray spectroscopy, X-ray diffraction, Brunauer–Emmett–Teller testing, and Raman spectroscopy. The effects of pyrolysis temperature and iron loading on RhB removal were investigated, and the optimum conditions of RhB removal were determined by reaction parameters: BC@nZVI dosage, PS concentration, pH values, reaction temperature, and inorganic anions in the BC@nZVI/PS system. Acidic and high-temperature conditions were more favorable for RhB removal. Additionally, free radical burst tests and electron paramagnetic resonance assays showed that $SO_4^{\bullet-}$ and $^{\bullet}OH$ were generated and worked in the removal process, while $SO_4^{\bullet-}$ is the main active species. BC@nZVI is an excellent catalyst for the treatment of RhB and provides an eco-friendly strategy for the treatment of organic pollutants in wastewater, with a broad application prospects.

Keywords: Organic pollutants; Biochar; BC@nZVI; Persulfate; Rhodamine B

1. Introduction

With the rapid development of industrialisation, organic wastewater discharges are increasing and the environmental problems caused by water pollution are becoming more and more serious. Rhodamine B (RhB), an organic pollutant in textile printing and dyeing wastewater, with the molecular formula of $C_{28}H_{31}N_2O_3Cl$, is a highly water soluble bright red fluorescent hetero-anthracene dye, which has been proven to be toxic effects on animals and humans [1]. Current treatment methods for pollutants in organic wastewater include activated carbon adsorption [2], Fenton oxidation [3], photocatalytic oxidation [4], and microbial degradation [5]. Although these methods are more effective in removing organic contaminants, the disadvantages of serious secondary pollution, high costs and energy consumption cannot be avoided [6].

Recently, advanced oxidation processes (AOPs) have been proven to be effective in the removal of various organic pollutants [7]. Advanced oxidation processes based on hydroxyl radicals ($^{\bullet}OH$) (E^0 = 1.8 ~ 2.7 V) are an effective technology for the removal of organic pollutants, while advanced oxidation processes based on sulfate radicals ($SO_4^{\bullet-}$) (E^0 = 2.5 ~ 3.1 V) have much higher oxidation capacity [8]. Compared to $^{\bullet}OH$, $SO_4^{\bullet-}$have a longer half-life, a wider pH tolerance, and are more selective than $^{\bullet}OH$ [9]. This means that $SO_4^{\bullet-}$ have a wider range of applications, allowing better contact and mass transfer between the catalyst and the target pollutant [10,11], and the above advantages

* Corresponding author.
† First authors.

of $SO_4^{\bullet-}$ ensure its better catalytic activity for the oxidation of toxic organic compounds. Many researchers have therefore produced $SO_4^{\bullet-}$ by activating persulfate (PS) to remove and mineralize hard-to-degrade pollutants. Typically, PS can be activated by heating [12], UV radiation [13], transition metal ions and metal oxidants [14,15], nano zero-valent iron (nZVI) [16], ultrasound, and alkalinization [17,18]. However, high energy inputs or the inevitable leaching of toxic metals limit its practical application.

Biochar (BC) is a cheap and readily available material made by pyrolysis of biomass in an anaerobic environment [19]. BC forms a porous structure during the pyrolysis process, and then shows a large surface area for many heavy metal ions and organic pollutants adsorption and excellent ion exchange capacity [20]. However, there are many problems in the application of biochar in wastewater, such as difficulty in separation and incomplete removal. Due to the advantages of cost-effective, efficient and environmentally friendly iron-based materials [21], and for the reason that the small particle size of nZVI, the large specific surface area and the high reactivity [22], many studies have used nZVI to activate PS and effectively produce $SO_4^{\bullet-}$ for removing organic pollutants [23,24]. However, nZVI tends to aggregate into micro-scale particles due to its high surface energy and intrinsic magnetic interactions [25], and is poorly stable and thermodynamically unstable in air, which reduces its activation performance [26]. To overcome these drawbacks, BC@nZVI was synthesized by loading nZVI on the surface of biochar [27]. As a compounds, BC@nZVI has the advantages of both BC and nZVI, thus it has the advantages of higher reduction or degradation efficiency, as well as easy recycling and non-agglomeration [28]. Abundant oxygen-containing functional groups, including hydroxyl (–OH) and carboxyl (–COOH) groups, can also be observed on the BC surface. These functional groups are able to activate PS with nZVI and show outstanding potential in the removal of organic pollutants from the environment [29]. Previous studies have shown that biochar loaded with nZVI not only increases the dispersibility of nZVI particles but also improves the removal efficiency of pollutants [30].

The zero-valent iron has been widely used as an activator for persulfates. Ghanbari et al. [31] have successfully prepared and used PDS/mZVI/aeration for the first time to degrade dye Acid Blue 9 (AB9). Tan et al. [32] prepared nZVI/CF-900-0.3 by one-step carbon thermal reduction in an inert gas atmosphere with high LEV degradation efficiency in the presence of PMS, and this catalyst showed excellent long-term stability after 6 months of storage. Pang et al. [33] investigated the degradation of Rhodamine B by ultrasound-assisted zero-valent iron corrosion-activated peroxymonosulfate. Under optimal conditions, 99.76% decolourisation of RhB was achieved within 12 min, and ZVI remained effective in activating PMS after 5 cycles of repeated use.

In the process of agricultural production, the waste rice husk is produced in huge quantities and will produce a lot of harmful gases that pollute the environment if it is disposed by incineration. Recycling the waste rice husk not only solves the pollution problem to a certain extent, but also increases the value of using rice husk. In contrast to the above-mentioned studies, we used agricultural waste rice husk as a source of biochar and synthesized BC@nZVI by high-temperature pyrolysis and carbothermal reduction, in which the iron compounds were reduced to nano zero-valent iron and the biomass was turned into biochar, and BC@nZVI was used to activate sodium persulfate for RhB removal. Biochar as a carrier of nano zero-valent iron has good stability and electrical conductivity, which effectively solves the problem that nano zero-valent iron is easy to agglomerate. And the biochar and nano-zero valent iron can synergistically activate the peroxynitrite's and improve the pollutant removal efficiency. In this study, the structure and morphology of the catalyst were characterized, the catalytic performance of the catalyst was analyzed and the effects of factors such as iron loading, pyrolysis temperature, PS concentration, catalyst dosage, pH, reaction temperature and interfering ions were investigated. This study provides a green and effective method for the removal of organic pollutants from wastewater.

2. Material and methods

2.1. Materials

Rice husk samples were taken from a local village in Shenyang, Liaoning Province, China. Chemicals including tert-butanol (TBA), methanol (MeOH), hydrochloric acid, sodium hydroxide, ferric chloride hexahydrate ($FeCl_3{\cdot}6H_2O$), anhydrous sodium sulfate, anhydrous sodium chloride, anhydrous sodium nitrate and sodium persulfate ($Na_2S_2O_8$). RhB ($C_{28}H_{31}N_2O_3Cl$) was used as the dye to simulate organic pollutants and was supplied by Shanghai Macklin Reagent Ltd., Co., (Shanghai, China).

All these chemicals were analytical grade and used without further purification. Distilled water was used to prepare the synthetic solutions of RhB as well as the other analytical solutions.

2.2. Catalyst synthesis

Rice husk powder with particle size less than 0.15 mm was used as raw material to prepare biochar. The $FeCl_3{\cdot}6H_2O$ (4.5, 6.0, 7.5, 10.5, and 15.0 mmol) was dissolved in 200 mL of deionized water, and 5.0 g of rice husk powder was added under magnetic stirring. After stirring for 24 h at room-temperature, put it into an oven and dried at 80°C for 24 h to obtain the Fe^{3+} impregnated rice husk powder.

The obtained Fe^{3+} impregnated straw powder was then to the tube furnace, and the temperature of the tube furnace was made to reach 700°C, 800°C, 900°C, and 1,000°C at a heating rate of 5°C/min under the condition of continuous high purity nitrogen gas. The insulation was kept for 4 h, and then naturally cooled to room temperature in the tube furnace.

2.3. Removal of RhB

The BC@nZVI and PS were added into 100 mL of RhB solution (10 mg/L). The effects of initial PS concentration (0, 0.5, 1.0, 1.5, and 2.0 mmol/L), catalyst dosage (0, 0.05, 0.075, 0.10, and 0.15 mg/L), pH value (3, 5, 7, 9, and 11), reaction temperature (20°C, 25°C, 30°C, and 35°C) and inorganic anion (Cl^-, NO_3^-, SO_4^{2-}) were investigated on the removal

efficiency of RhB. Quenching tests were carried out using TBA and MeOH as radical scavengers. Using 0.1 mol/L of HCl and NaOH adjust the pH of RhB solution. Fe^{2+} was determined by UV-VIS absorption spectrometry at 510 nm with 1,10-phenanthroline colorimetry and using hydroxylamine hydrochloride reduction Fe^{3+} to Fe^{2+} for determining total Fe.

The 250 mL conical flask was placed in a shaker with the speed 60 r/min, and a temperature of 25.0°C, 3.0 mL of suspension was extracted from the conical flask at a certain time intervals and filtered through a 0.45 μm filter membrane. Then the concentration of RhB was determined immediately. All experiments were repeated three times.

2.4. Material characterizations

The microstructure of the biochar and BC@nZVI were analyzed by scanning electron microscopy (SEM) (Quattro, Thermo Scientific, USA) coupled with energy-dispersive X-ray spectroscopy (EDS), to obtain surface elemental distribution maps by examining surface elemental composition. Raman spectrometer was used to record Raman spectrum at an excitation wavelength of 532 nm (BX41, Horiba, Japan). Automatic physical adsorption instrument was used to determine the specific surface area, pore volume, pore-size distribution (ASAP 2020, Micromeritics Instrument Corporation, USA). X-ray powder diffraction (XRD) patterns of the products were performed on X-ray diffractometer with Cu Kα radiation in the scattering angle 2θ range 10°C–90° (MiniFlex600, Rigaku, Japan). Active free radicals were identified by electron paramagnetic resonance (EPR) (EMXplus-10/12, Bruker, GER).

3. Result and discussion

3.1. XRD analysis

Fig. 1a shows the removal efficiency of RhB by the effect on pyrolysis temperatures of BC@nZVI. The final removal efficiency at different BC@nZVI (700°C, 800°C, 900°C, and 1,000°C) were 56.4%, 79.4%, 90.1%, and 93.1%, respectively. It can be seen that all four catalysts promote RhB removal, and BC@nZVI at high temperatures is more advantageous (BC@nZVI-1000 > BC@nZVI-900 > BC@nZVI-800 > BC@nZVI-700, respectively). The rise of pyrolysis temperature leads to the gradual conversion of Fe_3O_4 into nZVI, and the formation and conversion of nZVI affect the removal effect of RhB. Compared with nZVI, the removal effect of Fe_3O_4 on RhB is relatively weak.

To support these conclusions, XRD patterns was carried out to study the crystallization of BC and BC@nZVI synthesized at different pyrolysis temperature. Fig. 1b shows that all samples have diffraction peaks at characteristic positions and the existence of Fe varies at different pyrolysis temperatures. The broad diffraction peak at 20°~25° that matches well with the (002) face of the graphitic carbon [34], which is attributed to the amorphous biochar carbon [35], the degree of broadening of which is related to the amorphous structure [36]. When the temperature was 700°C, the iron in the pyrolysis product was mainly in the form of Fe_3O_4. When the temperature was increased to 800°C, 900°C, and 1,000°C, three diffraction peaks at 44.7°, 65.0°, and 82.3° match well with the (110), (200), and (211) faces of nZVI, respectively [37]. The intensity of the nZVI diffraction peaks increases sequentially with the increase of temperature, but the diffraction peaks of Fe_3O_4 still remain in the temperature of 900°C. At temperatures greater than or equal to 900°C, there are no diffraction peaks corresponding to Fe_3O_4 in the XRD spectra, indicating a better crystallinity of nZVI and a high purity of the nZVI obtained. When BC is loaded with nZVI, the intensity of the BC diffraction peak diminishes and the characteristics of BC and nZVI are reflected in specific positions of the BC@nZVI diffraction pattern, indicating the presence of nZVI in the synthesized nanomaterials, and BC@nZVI was successfully synthesized. Since the difference between BC@nZVI-900 and BC@nZVI-1000 was not significant for RhB removal efficiency, 900°C was chosen for subsequent experiments.

Fig. 2a shows the effect of different iron loadings on BC@nZVI for RhB removal. The removal efficiency of RhB at different iron impregnation concentration (0, 22.5, 30.0,

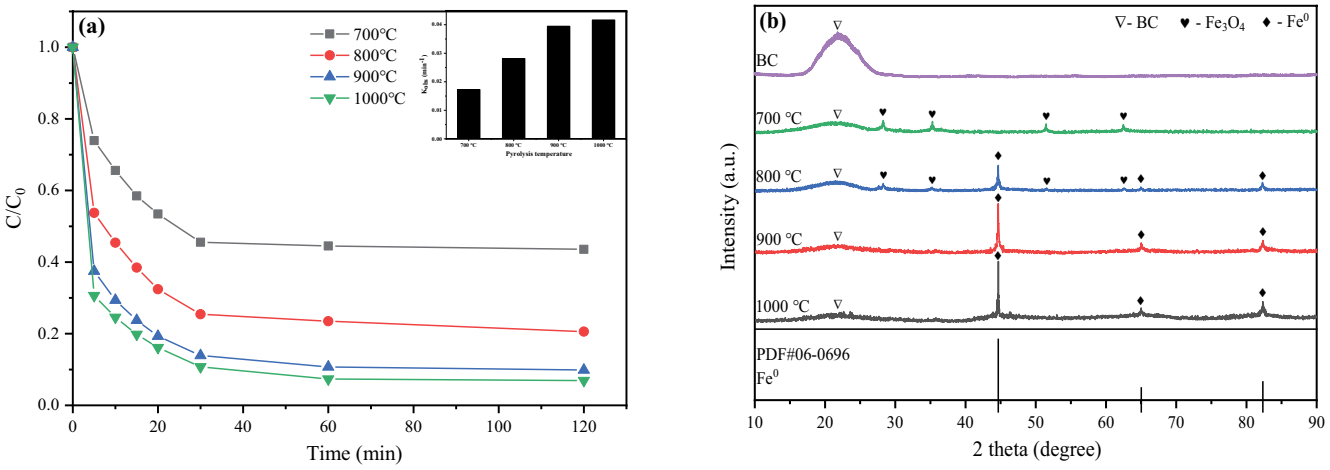

Fig. 1. Effect of pyrolysis temperatures on the removal efficiency of RhB (a); X-ray powder diffraction pattern of BC@nZVI at different pyrolysis temperatures (b). $[BC@nZVI]_0$ = 0.10 g/L, $[PS]_0$ = 1.0 mmol/L, $[RhB]_0$ = 10 mg/L, T = 298.0 K, pH = 6 ± 0.2.

37.5, 52.5, and 75.0 mmol/L) were 31.1%, 49.2%, 66.9%, 90.1%, 91.1%, and 84.7% and the reaction rate constants were 0.00492, 0.00852, 0.01648, 0.03948, 0.04033, and 0.02938 min^{-1}, respectively. It can be seen that the removal of RhB gradually increased with the iron impregnation concentration was increased from 22.5 to 52.2 mmol/L, but when the iron impregnation concentration was 75.0 mmol/L, the removal rate and the reaction rate constant of RhB decreased. This is because that more iron loading leads to an increase in nZVI agglomeration on the surface of BC [38], resulting in a decrease in the specific surface area of the material and removal efficiency.

Fig. 2b shows the XRD patterns of BC@nZVI made at 900°C with different iron loadings. All BC@nZVIs show distinctive diffraction peaks of nZVI and good crystallinity. The results indicate that the biomass could still reduce Fe compounds (Fe^{3+}) to nZVI. Furthermore, when other loading amounts of BC@nZVI were added, the resulting $SO_4^{\bullet-}$ reacted immediately with RhB, leading to an increase in the removal rate. However, adding BC@nZVI iron impregnation concentration of 75 mmol/L, excess Fe^{2+} [Eqs. (1) and (2)] [39] could be combined with $SO_4^{\bullet-}$ to produce SO_4^{2-} [Eq. (3)] [40], leading to a significant disappearance of $SO_4^{\bullet-}$ and a decrease in the RhB removal efficiency.

As there was little difference between the iron iron impregnation concentration of 37.5 and 52.5 mmol/L, the iron impregnation concentration of 37.5 mmol/L was chosen for subsequent experiments due to economic considerations.

$$2Fe^0 + O_2 + 2H_2O \rightarrow 2Fe^{2+} + 4OH^- \quad (1)$$

$$Fe^0 + 2H_2O \rightarrow Fe^{2+} + 2OH^- + H_2 \quad (2)$$

$$SO_4^{\bullet-} + Fe^{2+} \rightarrow Fe^{3+} + SO_4^{2-} \qquad k = 4.6 \times 10^9\ M^{-1}\cdot s^{-1} \quad (3)$$

3.2. Raman analysis

Raman spectroscopy can quickly and non-destructively characterize and differentiate the structure between various carbon-based materials. BC and BC@nZVI samples were selected for Raman spectroscopy testing and the results are shown in Fig. 3. The D-band at 1,350 cm^{-1} shows sp^3 hybridized carbon with structural defects, and the G-band at 1,570 cm^{-1} shows sp^2 hybridized carbon in the graphite structure [34]. The peak intensity ratio I_D/I_G of the D and G peaks can react to reflect the degree of defects and disorder in the carbon material [41]. The larger the value, the smaller the microcrystals on the surface of the sample, the greater the number of unsaturated carbon atoms on the surface and edge positions of the corresponding biochar, and thus the greater the reactivity of the surface. The I_D/I_G ratios of BC and BC@nZVI were 1.14 and 1.26, respectively, indicating that the degree of defective structure of biochar increased with the loading of nZVI. It also indicated that the sample material had a low degree of graphitization and an amorphous carbon structure with strong surface reactivity [42].

3.3. SEM analysis

The morphology of BC and BC@nZVI was characterized using SEM techniques. As shown in Fig. 4a and b, BC

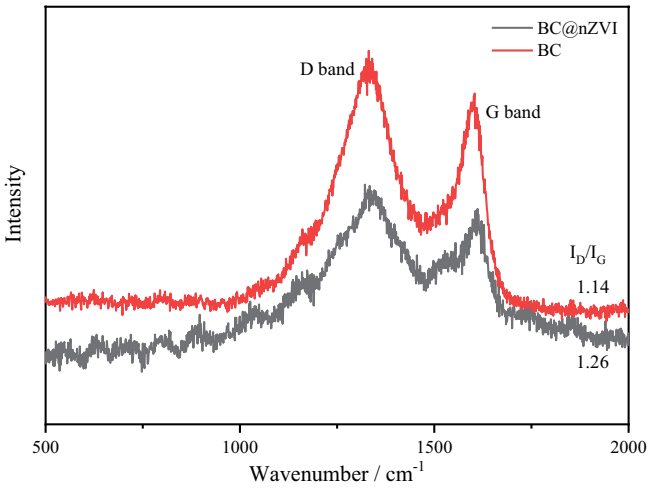

Fig. 3. Raman pattern of BC and BC@nZVI.

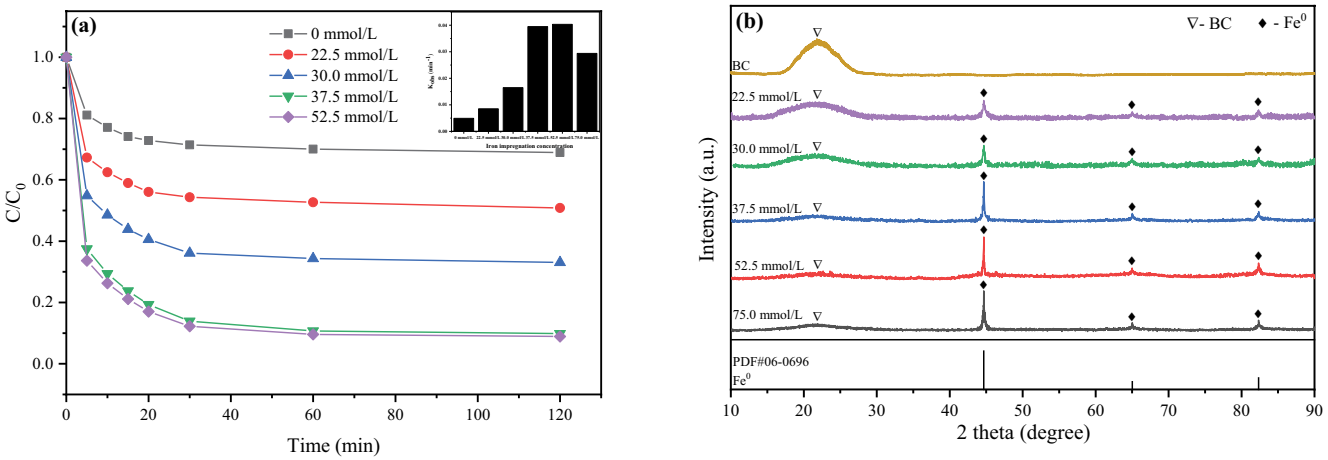

Fig. 2. Effect of different iron loads dosage on the removal efficiency of RhB (a); X-ray powder diffraction pattern of BC@nZVI with different iron loads at 900°C (b). $[BC@nZVI]_0$ = 0.10 g/L, $[PS]_0$ = 1.0 mmol/L, $[RhB]_0$ = 10 mg/L, T = 298.0 K, pH = 6 ± 0.2.

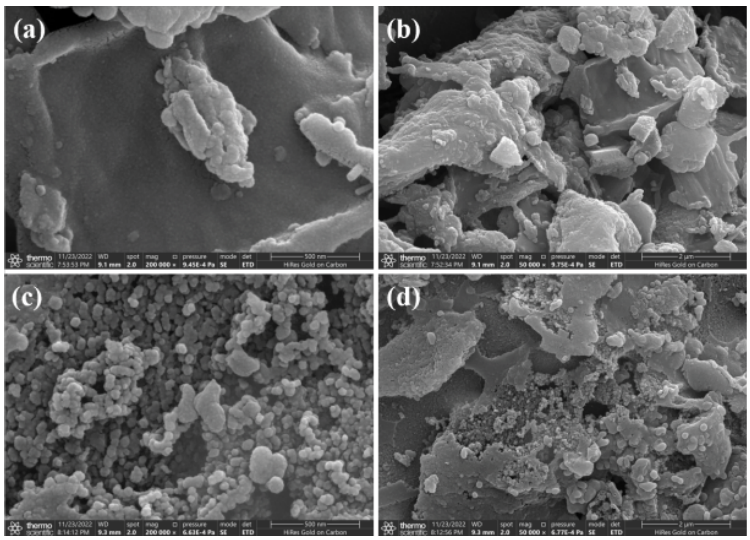

Fig. 4. Scanning electron microscopy images of BC (a, b) and BC@nZVI (c, d).

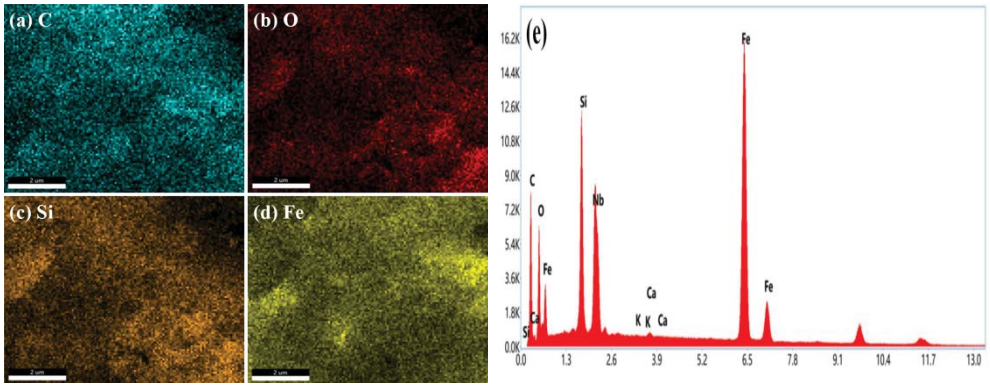

Fig. 5. Energy-dispersive X-ray spectroscopy mapping of BC@nZVI composite.

exhibits a smooth surface with a uniform lamellar structure. This lamellar structure and large specific surface area provide abundant active sites for nZVI immobilization and acts as an excellent carrier to prevent agglomeration of nZVI particles and facilitate the adsorption of pollutants.

The SEM images of BC@nZVI are shown in Fig. 4c and d. The nZVI particles are amorphous and dispersed on the surface of the biochar. The nZVI particle loading change the morphology and structural properties of BC, indicating that BC is an excellent solid dispersion, and maintain the stability and dispersion of nZVI, and improve the agglomeration resistance and catalytic activity of the composite.

The EDS elemental mapping identifies the surface elemental composition of BC@nZVI. As shown in Fig. 5, BC@nZVI catalyst contains mainly C (67.4%), Fe (11.2%) and O (15.2%), which further demonstrates the homogeneous distribution of the elements and the successful synthesis of the BC@nZVI composite. As biochar is a porous carbon with a high mineral content [43], it is worth noting that Si (3.6%), K (0.05%), Ca (0.1%) and Nb (2.5%) were also present in the catalyst. The above characterization visually explains the successful synthesis of BC@nZVI nanocomposites, which can successfully avoid aggregation of nZVI and may further show other good prospects.

3.4. Brunauer–Emmett–Teller analysis

The surface area and pore structure parameters of BC and BC@nZVI are listed in Table 1. The pore size of BC@nZVI is mainly distributed in 2~50 nm, which proves the mesoporous structure of BC@nZVI. The results show that BC has a larger surface area and a more porous structure. After loading nZVI onto the BC, SBET decreased slightly, indicating that the nZVI nanoparticles occupied some areas of the BC surface and porous. However, the total pore volume of BC@nZVI was larger than that of BC. Therefore, loading nZVI on BC improved the porous structure of BC@nZVI. The larger surface area and larger pore volume expand the contact area and facilitates Fenton-like reactions in the catalytic system.

3.5. Effect of PS concentration on the removal efficiency of RhB

The effect of PS concentration on RhB removal efficiency is shown in Fig. 6. In the absence of PS, the removal

Table 1
Surface structure characterization of different materials

Sample	BC	BC@nZVI
Brunauer–Emmett–Teller surface area (m^2/g)	683.444	648.947
Total pore volume (cm^3/g)	0.457535	0.525195
Micropore volume (cm^3/g)	0.304612	0.072550
Pore width (nm)	2.67782	3.23721

of RhB is mainly attributable to adsorption at BC@nZVI. The removal efficiency of RhB was 43.0% within 120 min. When the dosage of PS increased from 0 to 0.5 mmol/L, the removal efficiency was significantly accelerated. This phenomenon is due to the formation of $SO_4^{\bullet-}$ derived from PS. With the increase of PS concentration from 0.5 to 1.5 mmol/L, the removal efficiency of RhB increased from 70.4% to 97.0% within 120 min, indicating that the higher PS concentration was conducive to the removal of RhB. As PS is the source of $SO_4^{\bullet-}$, the increase of PS concentration promotes the generation of $SO_4^{\bullet-}$, thus promoting the removal efficiency of RhB. However, when the amount of PS increased to 2.0 mmol/L, the removal efficiency of RhB decreased. This may be due to reactions between ions in the solution or the consumption of $SO_4^{\bullet-}$ by PS [Eqs. (4) and (5)] [44]. The removal efficiency of RhB increased by 19.7% with the PS concentration increased from 0.5 to 1 mmol/L, but slowly changed (6.9%) when the PS concentration increased to 1.5 mmol/L. Thus, 1.0 mmol/L PS was selected as the best dosage for further experiment.

$$SO_4^{\bullet-} + SO_4^{\bullet-} = S_2O_8^{2-} \qquad k = 7\times10^8\ M^{-1}s^{-1} \tag{4}$$

$$S_2O_8^{2-} + SO_4^{\bullet-} = S_2O_8^{-} + SO_4^{2-} \tag{5}$$

3.6. Effect of BC@nZVI dosage on the removal efficiency of RhB

As shown in Fig. 7, the removal efficiency of RhB changed with BC@nZVI dosage. Previous studies have reported similar results, with increasing catalyst usage, catalytic activity increased [45,46]. In the absence of catalyst, RhB is difficult to be removed. With the increase of dosage from 0.05 to 0.1 g/L, the removal efficiency of RhB increased from 24.8% to 90.1% within 120 min. The removal efficiency of RhB was significantly improved, owing to the number of active sites increased with the increase of catalyst dose, resulting in the production of a large number of sulfate radicals attacking RhB chromophore. Adsorption is also conducive to this attack due to the larger contact surface availability on the catalyst [47]. With the further increase of catalyst to 0.15 g/L, its effect on RhB removal efficiency was weakened, possibly because excessive catalyst would produce scavenging effect and consume $SO_4^{\bullet-}$ [48].

3.7. Effect of pH values on the removal efficiency of RhB

Solution pH is an important factor in Fenton-like reaction process by metal leaching [48]. As shown in Fig. 8a, the

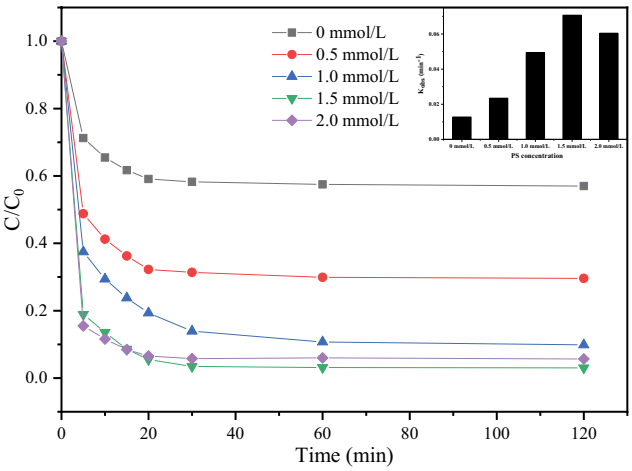

Fig. 6. Effect of PS concentration on the removal efficiency of RhB. $[BC@nZVI]_0$ = 0.10 g/L, $[RhB]_0$ = 10 mg/L, T = 25°C, pH = 6 ± 0.2.

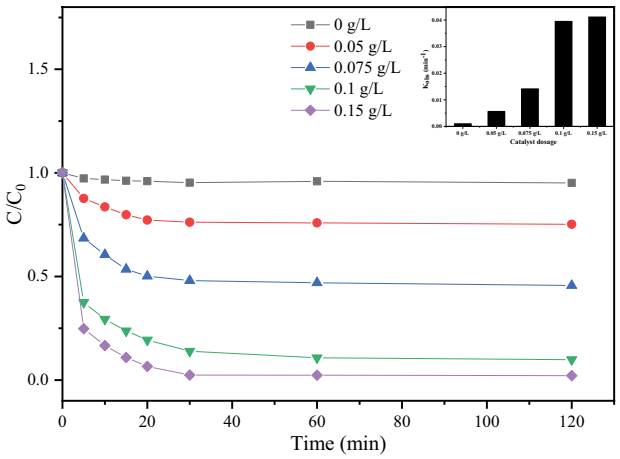

Fig. 7. Effect of BC@nZVI dosage on the removal efficiency of RhB (a); K_{obs} (b). $[PS]_0$ = 1.0 mmol/L, $[RhB]_0$ = 10 mg/L, T = 25°C, pH = 6 ± 0.2.

removal efficiency of RhB decreased with the increase of pH value. At pH = 3, 99.72% of RhB was removed for only 15 min, and the similar removal efficiency was obtained by Pang et al. [33] (12 min, 99.76%) under acid condition. At natural pH, the removal efficiency of RhB reached 90.1% at 120 min. The removal efficiency of RhB was 41.4% in pH = 11, in 120 min. Through kinetic equation calculation, the reaction rate constants are listed in Table 2, indicating that the acidic conditions had a more positive effect on the removal efficiency of RhB than the neutral and alkaline conditions. Furthermore, BC@nZVI was corroded to form Fe^{2+} as the activator of PS to generate under acidic conditions. With the decrease of pH value, the concentration of Fe^{2+} in the solution increases, and the removal efficiency correspondingly increased. According to the report, Fe^{2+} can be highly activated PS [49]. Dissolved Fe^{2+} play an important role in the activation of PS. At the same time, acidic conditions are

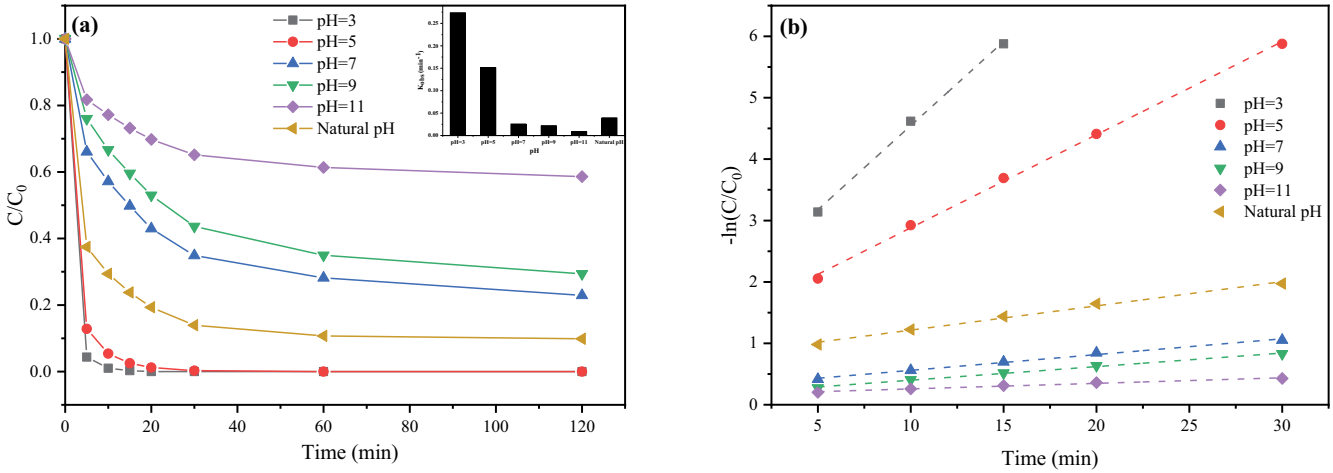

Fig. 8. Effect of pH values on the removal efficiency of RhB (a); corresponding kinetic curves of RhB with different pH values (b). $[BC@nZVI]_0$ = 0.10 g/L; $[PS]_0$ = 1.0 mmol/L, $[RhB]_0$ = 10 mg/L, T = 25°C.

Table 2
Kinetic parameters of RhB removal efficiency by different pH

Factors	Gradient	R^2	k (min^{-1})
pH	3	0.99575	0.27385
	5	0.99831	0.15167
	7	0.99144	0.02571
	9	0.99500	0.02211
	11	0.98096	0.00905
	Natural	0.99036	0.03948

conducive to the conversion of PS into $SO_4^{\bullet-}$ [Eq. (6)] [50]. Under acidic conditions, the enhanced removal efficiency of RhB may be due to the decreased activation energy required for PS activation and the accelerated activation process [51]. Under alkaline conditions, the catalytic performance of BC@nZVI reduced by the formation of iron oxide and iron hydroxide, which hinder the reaction of BC@nZVI with PS.

$$S_2O_8^{2-} + H^+ \rightarrow HS_2O_8^- \rightarrow SO_4^{\bullet-} + SO_4^{2-} + H^+ \quad (6)$$

3.8. Effect of temperature on the removal efficiency of RhB

Temperature is a key factor affecting non-homogeneous Fenton-like reactions. It has been reported that high temperature can activate PS to generate $SO_4^{\bullet-}$ by opening O–O bond [Eq. (7)] [52]. Therefore, batch experiments were conducted at different temperatures of 20°C, 25°C, 30°C, and 35°C to study the effect of temperature on the removal of RhB.

$$S_2O_8^{2-} + \text{heat} \rightarrow 2SO_4^{\bullet-} \quad (7)$$

As shown in Fig. 9a, the removal efficiency was significantly improved with the increase of temperature from 20°C to 35°C within 120 min (increased from 79.4% to 100%), the complete RhB removal was observed in 30 min at 35°C. As shown in Fig. 9b, RhB removal follows the pseudo-first-order kinetic equation. The kinetic rate constants of the RhB reaction at 20°C, 25°C, 30°C, and 35°C are shown in Table 3. And the fitting coefficients R^2 were over 0.99.

It can be seen that the removal efficiency was accelerated with the increase of temperature. Because higher temperature can increase the reaction rate of PS with the catalyst, and also increase the formation rate of $SO_4^{\bullet-}$. High catalytic activity at high temperature has also been reported [53]. However, high temperature increases operation cost for real application. Also, high temperature may have negative effects on the stability of catalysts, for example, destruction of biochar support and loss of active metals [54]. It is favorable for effective RhB removal at room temperature. Therefore, considering the practicability and convenience of removal rate, 25°C was selected for other experimental conditions.

3.9. Effect of inorganic anion on the removal efficiency of RhB

As we known, coexistence of inorganic anions is mainly in groundwater and industrial wastewater which will greatly reduce the removal efficiency of pollutants. In order to clarify the influence of inorganic anions on RhB removal, three common anions (Cl^-, NO_3^-, SO_4^{2-}) were added to the simulated wastewater to study their influence on the removal of RhB by BC@nZVI/PS system.

From Fig. 10, the anions have different degrees of influence on the removal of RhB from the BC@nZVI/PS system. Compared to the blank solution, the effect on removal increased in the order of $Cl^- < NO_3^- < SO_4^{2-}$. when Cl^-, NO_3^-, and SO_4^{2-} exists in 120 min, the removal efficiency of RhB decreased from 90.1% to 81.1%, 70.1% and 54.6%, respectively, due to the competition between Cl^-, NO_3^- and SO_4^{2-} on the catalyst surface and the adsorption of RhB molecules, resulting in a decrease in the removal efficiency [55].

Although Cl^- reacts with $SO_4^{\bullet-}$ and $^{\bullet}OH$, the effect of Cl^- is minimal, probably due to the large amount of chloride–reactive radicals ($^{\bullet}Cl$, $^{\bullet}Cl_2^-$ and $ClOH^{\bullet-}$) generated in solution by the reaction with $SO_4^{\bullet-}$ and $^{\bullet}OH$. These radicals can

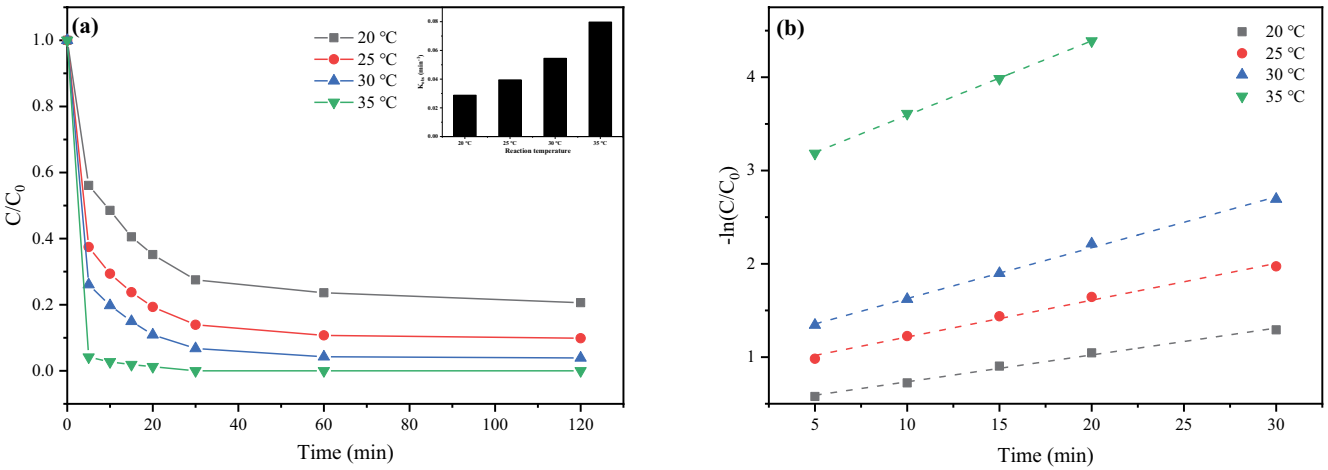

Fig. 9. Effect of temperature values on the removal efficiency of RhB (a); corresponding kinetic curves of RhB with different temperature values (b). $[BC@nZVI]_0$ = 0.10 g/L, $[PS]_0$ = 1.0 mmol/L, $[RhB]_0$ = 10 mg/L, pH = 6 ± 0.2.

Table 3
Kinetic parameters of RhB removal efficiency by different temperatures

Factors	Gradient	R^2	k (min^{-1})
Temperature	20°C	0.99249	0.02881
	25°C	0.99036	0.03948
	30°C	0.99691	0.05451
	35°C	0.99976	0.07976

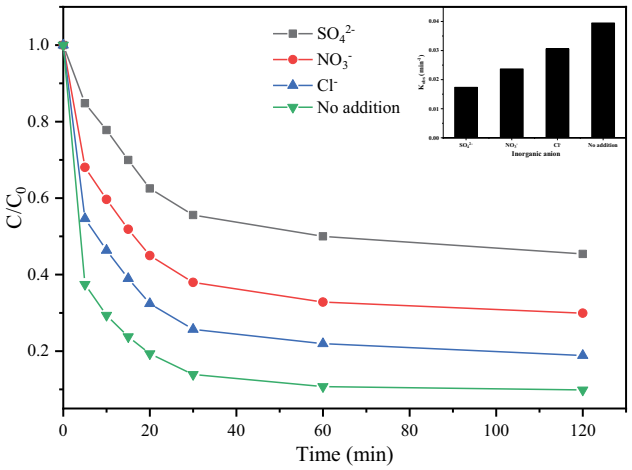

Fig. 10. Effect of inorganic anion on the removal efficiency of RhB. $[BC@nZVI]_0$ = 0.1 g/L, $[PS]_0$ = 1.0 mmol/L, $[RhB]_0$ = 10 mg/L, T = 25°C, pH = 6 ± 0.2.

compensate the consumption of $SO_4^{\bullet-}$ and $^{\bullet}OH$, thus leading to a slight reduction in the removal of RhB. RhB removal efficiency is slightly reduced [Eqs. (8)–(12)] [56,57]. NO_3^- is a competitive redox anion that oxidizes nZVI, and can be reduced to be NH_4^+, NO_2^-, $N_{2(g)}$, causing depletion of nZVI and inhibiting the removal efficiency of RhB [Eqs. (13)–(15)] [58]. On the other hand, SO_4^{2-} showed a strong inhibitory effect on the removal of RhB, probably due to the reaction of sulphate with nZVI to form iron sulphate deposited on the surface of BC@nZVI/PS, which hindered the activation of PS and reduced the removal efficiency of RhB. Studies have also confirmed that the presence of oxygen-containing anions in the solution hinders the normal progress of the reaction [59].

$$S_2O_8^{\bullet-} + Cl^- \rightarrow {}^{\bullet}Cl + SO_4^{2-} \qquad k = 3\times10^8 M^{-1}s^{-1} \tag{8}$$

$$^{\bullet}Cl + Cl^- \rightarrow Cl_2^- \tag{9}$$

$$^{\bullet}Cl_2^- + {}^{\bullet}Cl_2^- \rightarrow 2Cl^- + Cl_2 \tag{10}$$

$$^{\bullet}OH + Cl^- \rightarrow ClOH^{\bullet-} \qquad k = 4.3\times10^9 M^{-1}s^{-1} \tag{11}$$

$$ClOH^{\bullet-} + H^+ \rightarrow {}^{\bullet}Cl + H_2O \qquad k = 2.1\times10^{10} M^{-1}s^{-1} \tag{12}$$

$$4Fe^0 + NO_3^- + 10H^+ \rightarrow NH_4^+ + 4Fe^{2+} + 3H_2O \tag{13}$$

$$Fe^0 + NO_3^- + 2H^+ \rightarrow NO_2^- + Fe^{2+} + H_2O \tag{14}$$

$$5Fe^0 + 2NO_3^- + 12H^+ \rightarrow N_2(g) + 5Fe^{2+} + 6H_2O \tag{15}$$

3.10. Identification of reactive free radicals

During the conversion of persulfate, $SO_4^{\bullet-}$ and $^{\bullet}OH$ are generated, which affect the rate of non-homogeneous Fenton-like reactions. To further validate the reaction mechanism and to determine the type of radicals, EPR analysis was carried out using DMPO as the radical trap. The DMPO spin-capture EPR spectra of $SO_4^{\bullet-}$ and $^{\bullet}OH$ are shown in Fig. 11a. In the BC@nZVI/PS system, $SO_4^{\bullet-}$ and $^{\bullet}OH$ were produced, where the peak intensity of $SO_4^{\bullet-}$ was stronger than that of $^{\bullet}OH$, and $SO_4^{\bullet-}$ and $^{\bullet}OH$ co-existed in the reaction system.

The Fe^{2+} generated by BC@nZVI reacts with PS to form $SO_4^{\bullet-}$, and then reacts with H_2O or OH^- to form $^{\bullet}OH$ [Eqs. (16)–(18)] [40].

$$Fe^{2+} + S_2O_8^{2-} \rightarrow Fe^{3+} + SO_4^{2-} + SO_4^{\bullet-} \qquad k = 30\,M^{-1}s^{-1} \quad (16)$$

$$SO_4^{\bullet-} + H_2O \rightarrow SO_4^{2-} + {}^{\bullet}OH + H^+ \quad (17)$$

$$SO_4^{\bullet-} + OH^- \rightarrow SO_4^{2-} + {}^{\bullet}OH \quad (18)$$

To better analyze the degradation mechanism and identify the dominant radicals ($SO_4^{\bullet-}$ and $^{\bullet}OH$) during the degradation of RhB, MeOH or TBA were added to the reaction system as radical bursting agents. MeOH with α-hydrogen reacts with similar rate constants of 1.1×10^7 and 9.7×10^8 $M^{-1}\cdot s^{-1}$ for $SO_4^{\bullet-}$ and $^{\bullet}OH$, respectively, whereas TBA reacts with (6×10^8 $M^{-1}\cdot s^{-1}$) at a much faster rate than (8.4×10^5 $M^{-1}\cdot s^{-1}$) [60]. Therefore, MeOH and TBA can be used for the determination of the dominant radical in the system.

As shown in Fig. 11b, Both MeOH and TBA inhibited the degradation of RhB, and the removal efficiency of RhB decreased from 90.14% to 45.44% and 84.57%, respectively, within 120 min at natural pH. This shows that the $SO_4^{\bullet-}$ and $^{\bullet}OH$ were generated in BC@nZVI/PS system, and the $SO_4^{\bullet-}$ plays a more important role than the $^{\bullet}OH$.

3.11. Removal mechanism

Iron content in the nZVI/BC was determined as follow: 1.0 g of BC and BC@nZVI (37.5 mmol/L of iron impregnation concentration) were accurately weighed each in a crucible and then pyrolysised to ash at 600°C in muffle furnace. The resulting ashes were mixed with 30 mL of 1:1 hydrochloric acid and then shaken in a shaker for 2 h. The samples were then digested by heating in a water bath at 90°C for 20 min, and when the samples cooled down, they were filtered through a 0.45 μm filter membrane, and finally the iron content of the samples was determined by atomic absorption spectrophotometry. The iron content in BC@nZVI was obtained by calculating the difference of the iron content between BC@nZVI and BC. The obtained result is that 1.0 g of BC@nZVI with an iron impregnation concentration of 37.5 mmol/L contained 0.13 g of iron.

The BC@nZVI/PS system exhibits higher RhB removal efficiency than the BC/PS system, suggesting the loading of nZVI enhanced the PS-activating properties of BC. In addition, Fe measurements were carried out, as shown in Fig. 12. The concentration of Fe^{2+} increased gradually within 20 min, reached the peak and slowly decreased until equilibrium, while the concentration of Fe^{3+} maintained a slow increase until equilibrium. Meanwhile, the gradually increased concentration of total Fe (Fe(T)) can represent the leaching of the Fe ion concentration form nZVI/BC in the solution.

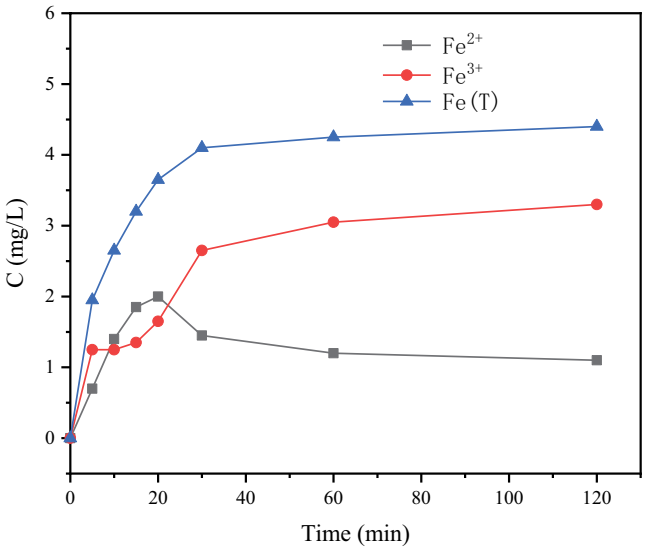

Fig. 12. Concentration of Fe^{2+} and Fe^{3+} in the BC@nZVI/PS system. $[BC@nZVI]_0$ = 0.1 g/L, $[PS]_0$ = 1.0 mmol/L, $[RhB]_0$ = 10 mg/L, T = 25°C, pH = 6 ± 0.2.

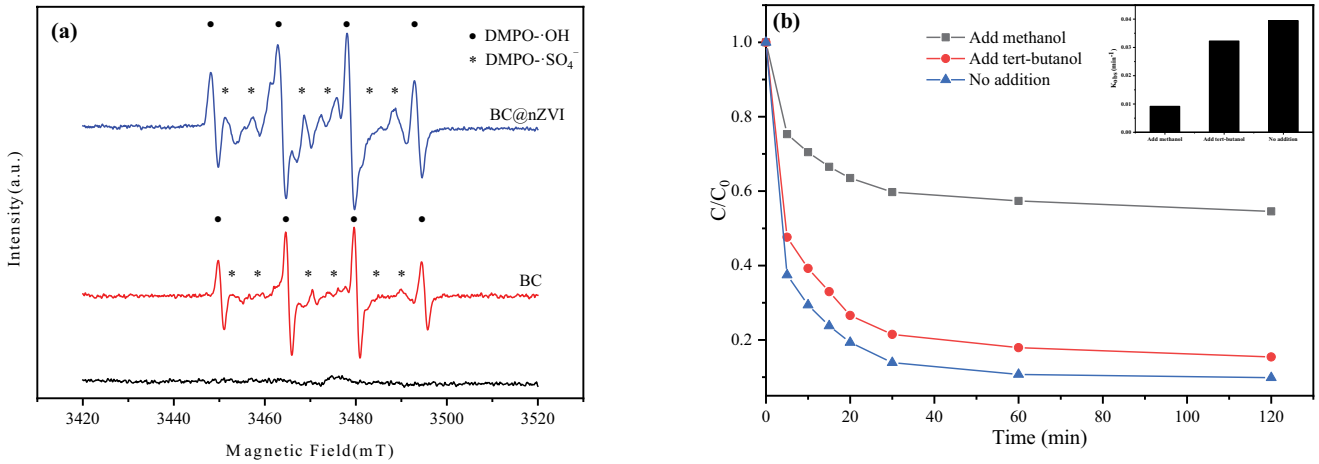

Fig. 11. EPR spectra of BC and BC@nZVI/PS system (a); effects of radical scavengers on RhB removal efficiency in BC@nZVI/PS system (b). $[BC@nZVI]_0$ = 0.1 g/L, $[PS]_0$ = 1.0 mmol/L, $[RhB]_0$ = 10 mg/L, T = 25°C, pH = 6 ± 0.2.

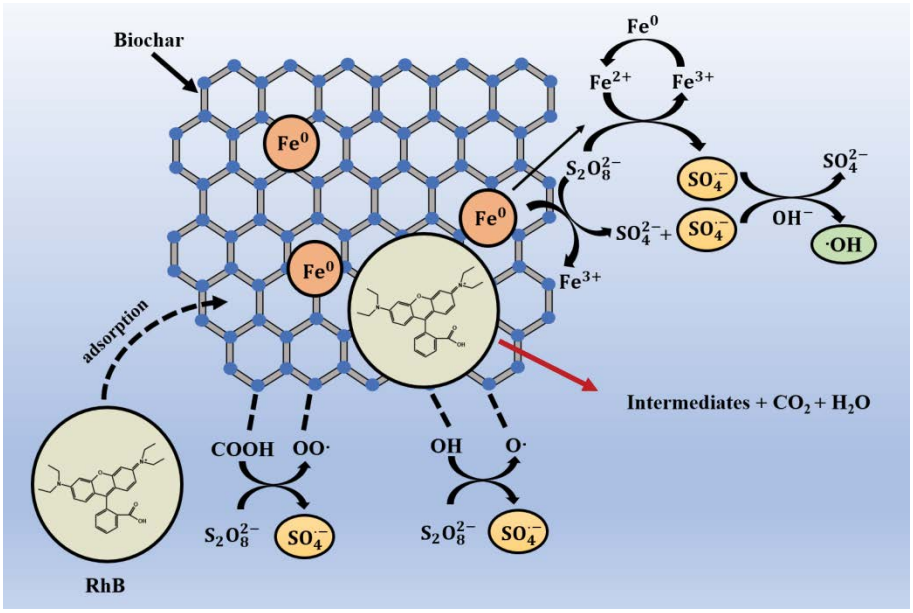

Fig. 13. Proposed mechanism of RhB removal by BC@nZVI/PS system.

The results show that in BC@nZVI/PS system, some of the nZVI is converted to dissolve Fe. In aqueous solution, nZVI can activate PS to form $SO_4^{\bullet-}$, $^{\bullet}OH$ and Fe^{2+} [Eqs. (19) and (20)] [40]. At the same time, the generated Fe^{2+} also reacts with $S_2O_8^{2-}$ to form $SO_4^{\bullet-}$ and Fe^{3+} [Eq. (16)]. Excess $SO_4^{\bullet-}$ may react with Fe^{2+} to form Fe^{3+} [Eq. (21)] [40]. As a result, the concentration of Fe^{2+} increases and then decreases until equilibrium, while the concentration of Fe^{3+} keeps increasing [61].

Based on these results, a mechanism of RhB removal is proposed (Fig. 13). BC is able to activate PS via the abundant containing oxygen functional groups (BC-OOH and BC-OH) on the BC surface, and release of $SO_4^{\bullet-}$ [Eqs. (22) and (23)] [62]. In addition, the structure of BC provides sufficient binding sites for nZVI, which facilitates the dispersion and full activation of nZVI particles. At the same time PS is activated by nZVI, producing $SO_4^{\bullet-}$ and a small amount of $^{\bullet}OH$ to degrade RhB [Eqs. (19 and (20)]. The concentration of Fe^{2+} in the water also gradually increases through the corrosion reaction of PS with nZVI. Then, Fe^{2+} activates PS to produce $SO_4^{\bullet-}$ through an electron transfer process [Eq. (16)]. Fe^{3+} in the pores of the BC@nZVI material can react with nZVI to regenerate Fe^{2+} [Eq. (24)] [40]. The pH then gradually drops due to the decomposition of PS and the release of H^+ into the system [Eq. (25)] [63]. Acidic aqueous conditions also favour the production of Fe^{2+}. In addition, $SO_4^{\bullet-}$ can react with H_2O to form $^{\bullet}OH$ [Eq. (26)] [64]. During the reaction, the large specific surface area of BC@nZVI allows RhB to be concentrated near its surface or within its pores, facilitating the contact reaction between the pollutant and the active species. Fig. 13 shows the possible mechanisms for the removal of RhB in the BC@nZVI/PS system include adsorption, homogeneous and non-homogeneous Fenton reactions [65]. According to the previous study, the destruction of RhB via N-de-ethylation, chromophore cleavage and ring open reactions, and finally mineralize into CO_2 and H_2O [66].

$$Fe^0 + 2S_2O_8^{2-} \rightarrow Fe^{2+} + 2SO_4^{2-} + 2SO_4^{\bullet-} \quad (19)$$

$$Fe^0 + S_2O_8^{2-} + 2H_2O \rightarrow 2SO_4^{2-} + Fe^{2+} + 2^{\bullet}OH + 2H^+ \quad (20)$$

$$SO_4^{\bullet-} + Fe^{2+} \rightarrow S_2O_8^{2-} + Fe^{3+} \qquad k = 4.6\times10^9\ M^{-1}s^{-1} \quad (21)$$

$$BC\text{-}OOH + S_2O_8^{2-} \rightarrow {}^{\bullet}BC\text{-}OO + SO_4^{\bullet-} + HSO_4^- \quad (22)$$

$$BC\text{-}OH + S_2O_8^{2-} \rightarrow {}^{\bullet}BC\text{-}O + SO_4^{\bullet-} + HSO_4^- \quad (23)$$

$$Fe^{3+} + Fe^0 \rightarrow 2Fe^{2+} \quad (24)$$

$$S_2O_8^{2-} + 2H_2O \rightarrow HO_2^- + 2SO_4^{2-} + 3H^+ \quad (25)$$

$$SO_4^{\bullet-} + H_2O \rightarrow SO_4^{2-} + {}^{\bullet}OH + H^+ \quad (26)$$

4. Conclusions

In this study, BC@nZVI was prepared by co-heating rice husk powder with ferric chloride, and used as an activator for removing RhB from wastewater. The physico-chemical properties were characterized. According to the experimental results, the optimum pyrolysis temperature is 900°C and the iron impregnation concentration is 37.5 mmol/L. The nZVI loaded on the surface of BC enhanced the redox effect between Fe^{2+} and Fe^{3+} and promoted the production of $SO_4^{\bullet-}$, and low pyrolysis temperature and high loading of Fe were detrimental to RhB removal. BC@nZVI dosage, PS concentration, inorganic anions, initial pH, and temperature had different degrees of influence on RhB removal. The results showed that low pH and high temperature were beneficial to the removal of RhB. At natural pH (pH = 6 ± 0.2) and room temperature (25°C), the removal efficiency of

RhB was up to 90.1% within 120 min. The mechanism of PS activation by BC@nZVI was investigated using EPR and quenching experiments. The results showed that both $^{\bullet}SO_4^-$ and $^{\bullet}OH$ played a positive role in BC@nZVI/PS system, but the $^{\bullet}SO_4^-$ radical was the dominant species. Overall, the BC@nZVI was successfully prepared in this study, and is a promising PS activation material with great potential for application in the decomposition of organic pollutants and environmental remediation.

Funding

This project was supported by Liaoning Province Education Administration (No. LJ2020008, LQ2020023, and LQ2020027). Program for Liaoning Innovative Research Team in University (LT2020).

Competing interests

The authors have no relevant financial or non-financial interests to disclose.

Data availability

All data generated or analyzed during this study are included in this article.

References

[1] L.S. Kong, G.D. Fang, Y.F. Chen, M. Xie, F. Zhu, L. Ma, D.M. Zhou, J.H. Zhan, Efficient activation of persulfate decomposition by Cu_2FeSnS_4 nanomaterial for bisphenol A degradation: kinetics, performance and mechanism studies, Appl. Catal., B, 253 (2019) 278–285.
[2] T. Zhang, X.S. Wu, S.M. Shaheen, Q. Zhao, X.J. Liu, J. Rinklebe, H.Q. Ren, Ammonium nitrogen recovery from digestate by hydrothermal pretreatment followed by activated hydrochar sorption, Chem. Eng. J., 379 (2020) 122254, doi: 10.1016/j.cej.2019.122254.
[3] G.Q. Zhou, Z.W. Chen, F. Fang, Y.F. He, H.L. Sun, H.X. Shi, Fenton-like degradation of Methylene Blue using paper mill sludge-derived magnetically separable heterogeneous catalyst: characterization and mechanism, J. Environ. Sci. (China), 35 (2015) 20–26.
[4] L. Wang, D.W. Bahnemann, L. Bian, G.H. Dong, J. Zhao, C.Y. Wang, Two-dimensional layered zinc silicate nanosheets with excellent photocatalytic performance for organic pollutant degradation and CO_2 conversion, Angew. Chem. Int. Ed., 58 (2019) 8103–8108.
[5] Q.H. Ye, C.Y. Liang, X.W. Chen, T.T. Fang, Y. Wang, H. Wang, Molecular characterization of methanogenic microbial communities for degrading various types of polycyclic aromatic hydrocarbon, J. Environ. Sci. (China), 86 (2019) 97–106.
[6] S. Guo, Z.X. Yang, Z.P. Wen, H. Fida, G.K. Zhang, J.Y. Chen, Reutilization of iron sludge as heterogeneous Fenton catalyst for the degradation of Rhodamine B: role of sulfur and mesoporous structure, J. Colloid Interface Sci., 532 (2018) 441–448.
[7] G. Ayoub, A. Ghauch, Assessment of bimetallic and trimetallic iron-based systems for persulfate activation: application to sulfamethoxazole degradation, Chem. Eng. J., 256 (2014) 280–292.
[8] P. Devi, U. Das, A.K. Dalai, *In-situ* chemical oxidation: principle and applications of peroxide and persulfate treatments in wastewater systems, Sci. Total Environ., 571 (2016) 643–657.
[9] D.N. Zhou, H. Zhang, L. Chen, Sulfur-replaced Fenton systems: can sulfate radical substitute hydroxyl radical for advanced oxidation technologies?, J. Chem. Technol. Biotechnol., 90 (2015) 775–779.
[10] Y.Y. Fu, S.N. Li, Y.F. Shi, J.J. Geng, J.C. Li, G. Wu, K. Xu, H.Q. Ren, Removal of artificial sweeteners using UV/persulfate: radical-based degradation kinetic model in wastewater, pathways and toxicity, Water Res., 167 (2019) 115102, doi: 10.1016/j.watres.2019.115102.
[11] M.B. Gu, Q. Sui, U. Farooq, X. Zhang, Z.F. Qiu, S.G. Lyu, Degradation of phenanthrene in sulfate radical based oxidative environment by nZVI-PDA functionalized rGO catalyst, Chem. Eng. J., 354 (2018) 541–552.
[12] Y.X. Zhang, H.L. Liu, Y.J. Xin, Y.P. Shen, J. Wang, C. Cai, M.M. Wang, Erythromycin degradation and ERY-resistant gene inactivation in erythromycin mycelial dreg by heat-activated persulfate oxidation, Chem. Eng. J., 358 (2019) 1446–1453.
[13] E.A. Serna-Galvis, F. Ferraro, J. Silva-Agredo, R.A. Torres-Palma, Degradation of highly consumed fluoroquinolones, penicillins and cephalosporins in distilled water and simulated hospital wastewater by UV_{254} and UV_{254}/persulfate processes, Water Res., 122 (2017) 128–138.
[14] P.H. Shi, R.J. Su, F.Z. Wan, M.C. Zhu, D.X. Li, S.H. Xu, Co_3O_4 nanocrystals on graphene oxide as a synergistic catalyst for degradation of Orange II in water by advanced oxidation technology based on sulfate radicals, Appl. Catal., B, 123–124 (2012) 265–272.
[15] J. Zou, J. Ma, L.W. Chen, X.C. Li, Y.H. Guan, P.C. Xie, C. Pan, Rapid acceleration of ferrous iron/peroxymonosulfate oxidation of organic pollutants by promoting Fe(III)/Fe(II) cycle with hydroxylamine, Environ. Sci. Technol., 47 (2013) 11685–11691.
[16] H.R. Dong, Q. Ning, L. Li, Y.Y. Wang, B. Wang, L.H. Zhang, R. Tian, R. Li, J. Chen, Q.Q. Xie, A comparative study on the activation of persulfate by bare and surface-stabilized nanoscale zero-valent iron for the removal of sulfamethazine, Sep. Purif. Technol., 230 (2020) 115869, doi: 10.1016/j.seppur.2019.115869.
[17] L.W. Matzek, K.E. Carter, Activated persulfate for organic chemical degradation: a review, Chemosphere, 151 (2016) 178–188.
[18] G. Boczkaj, A. Fernandes, Wastewater treatment by means of advanced oxidation processes at basic pH conditions: a review, Chem. Eng. J., 320 (2017) 608–633.
[19] D. O'Connor, T.Y. Peng, J.L. Zhang, D.C.W. Tsang, D.S. Alessi, Z.T. Shen, N.S. Bolan, D.Y. Hou, Biochar application for the remediation of heavy metal polluted land: a review of *in-situ* field trials, Sci. Total Environ., 619–620 (2018) 815–826.
[20] X.F. Tan, Y.G. Liu, G.M. Zeng, X. Wang, X.J. Hu, Y.L. Gu, Z.Z. Yang, Application of biochar for the removal of pollutants from aqueous solutions, Chemosphere, 125 (2015) 70–85.
[21] Y.J. Xiang, Z.Y. Xu, Y.Y. Zhou, Y.Y. Wei, X.Y. Long, Y.Z. He, D. Zhi, J. Yang, L. Luo, A sustainable ferromanganese biochar adsorbent for effective levofloxacin removal from aqueous medium, Chemosphere, 237 (2019) 124464, doi: 10.1016/j.chemosphere.2019.124464.
[22] F. Yang, S.S. Zhang, Y.Q. Sun, K. Cheng, J.S. Li, D.C.W. Tsang, Fabrication and characterization of hydrophilic corn stalk biochar-supported nanoscale zero-valent iron composites for efficient metal removal, Bioresour. Technol., 265 (2018) 490–497.
[23] S.-Y. Oh, S.-G. Kang, D.-W. Kim, P.C. Chiu, Degradation of 2,4-dinitrotoluene by persulfate activated with iron sulfides, Chem. Eng. J., 172 (2011) 641–646.
[24] I. Hussain, Y.Q. Zhang, S.B. Huang, X.Z. Du, Degradation of *p*-chloroaniline by persulfate activated with zero-valent iron, Chem. Eng. J., 203 (2012) 269–276.
[25] T. Phenrat, N. Saleh, K. Sirk, R.D. Tilton, G.V. Lowry, Aggregation and sedimentation of aqueous nanoscale zerovalent iron dispersions, Environ. Sci. Technol., 41 (2007) 284–290.
[26] Y. Dai, Y.C. Hu, B.J. Jiang, J.L. Zou, G.H. Tian, H.G. Fu, Carbothermal synthesis of ordered mesoporous carbon-supported nano zero-valent iron with enhanced stability and activity for hexavalent chromium reduction, J. Hazard. Mater., 309 (2016) 249–258.

[27] S.S. Li, F. Yang, J.S. Li, K. Cheng, Porous biochar-nanoscale zero-valent iron composites: synthesis, characterization and application for lead ion removal, Sci. Total Environ., 746 (2020) 141037, doi: 10.1016/j.scitotenv.2020.141037.
[28] H.W. Luo, Y.F. Zeng, D.Q. He, X.L. Pan, Application of iron-based materials in heterogeneous advanced oxidation processes for wastewater treatment: a review, Chem. Eng. J., 407 (2021) 127191, doi: 10.1016/j.cej.2020.127191.
[29] S.Y. Yang, X. Yang, X.T. Shao, R. Niu, L.L. Wang, Activated carbon catalyzed persulfate oxidation of Azo dye acid orange 7 at ambient temperature, J. Hazard. Mater., 186 (2011) 659–666.
[30] S. Mandal, S.Y. Pu, L.X. Shangguan, S.B. Liu, H. Ma, S. Adhikari, D.Y. Hou, Synergistic construction of green tea biochar supported nZVI for immobilization of lead in soil: a mechanistic investigation, Environ. Int., 135 (2020) 105374, doi: 10.1016/j.envint.2019.105374.
[31] F. Ghanbari, M. Riahi, B. Kakavandi, X.T. Hong, K.-Y. Andrew Lin, Intensified peroxydisulfate/microparticles-zero valent iron process through aeration for degradation of organic pollutants: kinetic studies, mechanism and effect of anions, J. Water Process Eng., 36 (2020) 101321, doi: 10.1016/j.jwpe.2020.101321.
[32] W.T. Tan, Y. Ruan, Z.H. Diao, G. Song, M.H. Su, L.A. Hou, D.Y. Chen, L.J. Kong, H.M. Deng, Removal of levofloxacin through adsorption and peroxymonosulfate activation using carbothermal reduction synthesized nZVI/carbon fiber, Chemosphere, 280 (2021) 130629, doi: 10.1016/j.chemosphere.2021.130626.
[33] Y.X. Pang, Y. Ruan, Y. Feng, Z.H. Diao, K. Shih, L.A. Hou, D.Y. Chen, L.J. Kong, Ultrasound assisted zero valent iron corrosion for peroxymonosulfate activation for Rhodamine B degradation, Chemosphere, 228 (2019) 412–417.
[34] P. Cheng, T. Li, H. Yu, L. Zhi, Z.H. Liu, Z.B. Lei, Biomass-derived carbon fiber aerogel as a binder-free electrode for high-rate supercapacitors, J. Phys. Chem. C, 120 (2016) 2079–2086.
[35] P. Zhang, X.F. Tan, S.B. Liu, Y.G. Liu, G.G. Zeng, S.J. Ye, Z.H. Yin, X.J. Hu, N. Liu, Catalytic degradation of estrogen by persulfate activated with iron-doped graphitic biochar: process variables effects and matrix effects, Chem. Eng. J., 378 (2019) 122141, doi: 10.1016/j.cej.2019.122141.
[36] I. Hussain, M.Y. Li, Y.Q. Zhang, Y.C. Li, S.B. Huang, X.D. Du, G.Q. Liu, W. Hayat, N. Anwar, Insights into the mechanism of persulfate activation with nZVI/BC nanocomposite for the degradation of nonylphenol, Chem. Eng. J., 311 (2017) 163–172.
[37] S.F. Li, T.T. You, Y. Guo, S.H. Yao, S.Y. Zang, M. Xiao, Z.G. Zhang, Y.M. Shen, High dispersions of nano zero valent iron supported on biochar by one-step carbothermal synthesis and its application in chromate removal, RSC Adv., 9 (2019) 12428–12435.
[38] J.J. Chen, J.X. Zhu, Z.L. Da, H. Xu, J. Yan, H.Y. Ji, H.M. Shu, H.M. Li, Improving the photocatalytic activity and stability of graphene-like BN/AgBr composites, Appl. Surf. Sci., 313 (2014) 1–9.
[39] J.C. Yan, L. Han, W.G. Gao, S. Xue, M.F. Chen, Biochar supported nanoscale zerovalent iron composite used as persulfate activator for removing trichloroethylene, Bioresour. Technol., 175 (2015) 269–274.
[40] A. Hassani, J. Scaria, F. Ghanbari, P.V. Nidheesh, Sulfate radicals-based advanced oxidation processes for the degradation of pharmaceuticals and personal care products: a review on relevant activation mechanisms, performance, and perspectives, Environ. Res., 217 (2023) 114789, doi: 10.1016/j.envres.2022.114789.
[41] H. Liu, P. Sun, M.B. Feng, H.X. Liu, S.G. Yang, L.S. Wang, Z.Y. Wang, Nitrogen and sulfur co-doped CNT-COOH as an efficient metal-free catalyst for the degradation of UV filter BP-4 based on sulfate radicals, Appl. Catal., B, 187 (2016) 1–10.
[42] M.T. Zheng, Y.L. Liu, Y. Xiao, Y. Zhu, Q. Guan, D.S. Yuan, J.X. Zhang, An easy catalyst-free hydrothermal method to prepare monodisperse carbon microspheres on a large scale, J. Phys. Chem. C, 113 (2009) 8455–8459.
[43] L.B. Qian, W.Y. Zhang, J.C. Yan, L. Han, Y. Chen, D. Ouyang, M.F. Chen, Nanoscale zero-valent iron supported by biochars produced at different temperatures: synthesis mechanism and effect on Cr(VI) removal, Environ. Pollut., 223 (2017) 153–160.
[44] N. Yousefi, S. Pourfadakari, S. Esmaeili, A.A. Babaei, Mineralization of high saline petrochemical wastewater using sonoelectro-activated persulfate: degradation mechanisms and reaction kinetics, Microchem. J., 147 (2019) 1075–1082.
[45] J.-H. Chu, J.-K. Kang, S.-J. Park, C.-G. Lee, Application of magnetic biochar derived from food waste in heterogeneous sono-Fenton-like process for removal of organic dyes from aqueous solution, J. Water Process Eng., 37 (2020) 101455, doi: 10.1016/j.jwpe.2020.101455.
[46] Y.X. Xie, X.Q. Wang, W.H. Tong, W.R. Hu, P.Y. Li, L.L. Dai, Y.B. Wang, Y.K. Zhang, FexP/biochar composites induced oxygen-driven Fenton-like reaction for sulfamethoxazole removal: performance and reaction mechanism, Chem. Eng. J., 396 (2020) 125321, doi: 10.1016/j.cej.2020.125321.
[47] K.K. Rubeena, P. Hari Prasad Reddy, A.R. Laiju, P.V. Nidheesh, Iron impregnated biochars as heterogeneous Fenton catalyst for the degradation of acid red 1 dye, J. Environ. Manage., 226 (2018) 320–328.
[48] G.F. Liu, Y.Y. Zhang, H.L. Yu, R.F. Jin, J.T. Zhou, Acceleration of goethite-catalyzed Fenton-like oxidation of ofloxacin by biochar, J. Hazard. Mater., 397 (2020) 122783, doi: 10.1016/j.jhazmat.2020.122783.
[49] G. Barzegar, S. Jorfi, V. Zarezade, M. Khatebasreh, F. Mehdipour, F. Ghanbari, 4-Chlorophenol degradation using ultrasound/peroxymonosulfate/nanoscale zero valent iron: reusability, identification of degradation intermediates and potential application for real wastewater, Chemosphere, 201 (2018) 370–379.
[50] C.L. Jiang, Y.F. Ji, Y.Y. Shi, J.F. Chen, T.M. Cai, Sulfate radical-based oxidation of fluoroquinolone antibiotics: kinetics, mechanisms and effects of natural water matrices, Water Res., 106 (2016) 507–517.
[51] K.E. Manz, T.J. Adams, K.E. Carter, Furfural degradation through heat-activated persulfate: impacts of simulated brine and elevated pressures, Chem. Eng. J., 353 (2018) 727–735.
[52] M.H. Nie, Y. Yang, Z.J. Zhang, C.X. Yan, X.N. Wang, H.J. Li, W.B. Dong, Degradation of chloramphenicol by thermally activated persulfate in aqueous solution, Chem. Eng. J., 246 (2014) 373–382.
[53] C.Q. Wang, Y.J. Cao, H. Wang, Copper-based catalyst from waste printed circuit boards for effective Fenton-like discoloration of Rhodamine B at neutral pH, Chemosphere, 230 (2019) 278–285.
[54] H. Titouhi, J.-E. Belgaied, Heterogeneous Fenton oxidation of ofloxacin drug by iron alginate support, Environ. Technol., 37 (2016) 2003–2015.
[55] I. Epold, M. Trapido, N. Dulova, Degradation of levofloxacin in aqueous solutions by Fenton, ferrous ion-activated persulfate and combined Fenton/persulfate systems, Chem. Eng. J., 279 (2015) 452–462.
[56] T.H. Xi, X.D. Li, Q.H. Zhang, N. Liu, S. Niu, Z.J. Dong, C. Lyu, Enhanced catalytic oxidation of 2,4-dichlorophenol via singlet oxygen dominated peroxymonosulfate activation on CoOOH@Bi_2O_3 composite, Front. Environ. Sci. Eng., 15 (2021) 55, doi: 10.1007/s11783-020-1347-5.
[57] G. Barzegar, M. Sabaghan, O. Azadbakht, E. Aghayani, M. Mahdavianpour, A. Kadier, S. Fallahizadeh, F. Ghanbari, Ciprofloxacin degradation by catalytic activation of monopersulfate using Mn–Fe oxides: performance and mineralization, Water Sci. Technol., 87 (2023) 1029–1042.
[58] J.F. Li, Y.M. Li, Q.L. Meng, Removal of nitrate by zero-valent iron and pillared bentonite, J. Hazard. Mater., 174 (2010) 188–193.
[59] T. Wang, J. Su, X.Y. Jin, Z.L. Chen, M. Megharaj, R. Naidu, Functional clay supported bimetallic nZVI/Pd nanoparticles used for removal of methyl orange from aqueous solution, J. Hazard. Mater., 262 (2013) 819–825.
[60] J.C. Yan, M. Lei, L.H. Zhu, M.N. Anjum, J. Zou, H.Q. Tang, Degradation of sulfamonomethoxine with Fe_3O_4 magnetic

nanoparticles as heterogeneous activator of persulfate, J. Hazard. Mater., 186 (2011) 1398–1404.
[61] F. Zhu, Y.Y. Wu, Y.K. Liang, H.H. Li, W.J. Liang, Degradation mechanism of norfloxacin in water using persulfate activated by BC@nZVI/Ni, Chem. Eng. J., 389 (2020) 124276, doi: 10.1016/j.cej.2020.124276.
[62] L.C. Zhou, J.J. Ma, H. Zhang, Y.M. Shao, Y.F. Li, Fabrication of magnetic carbon composites from peanut shells and its application as a heterogeneous Fenton catalyst in removal of methylene blue, Appl. Surf. Sci., 324 (2015) 490–498.
[63] C. Kim, J.Y. Ahn, T.Y. Kim, W.S. Shin, I. Hwang, Activation of persulfate by nanosized zero-valent iron (nZVI): mechanisms and transformation products of nZVI, Environ. Sci. Technol., 52 (2018) 3625–3633.
[64] H.Z. Liu, T.A. Bruton, W. Li, J.V. Buren, C. Prasse, F.M. Doyle, D.L. Sedlak, Oxidation of benzene by persulfate in the presence of Fe(III)- and Mn(IV)-containing oxides: stoichiometric efficiency and transformation products, Environ. Sci. Technol., 50 (2016) 890–898.
[65] Q. Gan, H.J. Hou, S. Liang, J.J. Qiu, S.Y. Tao, L. Yang, W.B. Yu, K.K. Xiao, B.C. Liu, J.P. Hu, Y.F. Wang, J.K. Yang, Sludge-derived biochar with multivalent iron as an efficient Fenton catalyst for degradation of 4-chlorophenol, Sci. Total Environ., 725 (2020) 138299, doi: 10.1016/j.scitotenv.2020.138299.
[66] R.Z. Xie, Y.B. Jiang, A. Armutlulu, Z.Y. Shen, B. Lai, H. Wang, One-step fabrication of oxygen vacancy-enriched Fe@Ti/C composite for highly efficient degradation of organic pollutants through persulfate activation, J. Colloid Interface Sci., 583 (2021) 394–403.